

Ultrafast Orbital-Selective Photodoping Melts Charge Order in Overdoped Bi-based Cuprates

Xinyi Jiang,^{1,*} Qizhi Li,^{1,*} Qingzheng Qiu,¹ Li Yue,¹ Junhan Huang,¹ Yiwen Chen,² Byungjune Lee,^{3,4} Hyeongi Choi,⁵ Xingjiang Zhou,² Tao Dong,¹ Nanlin Wang,¹ Hoyoung Jang,^{5,6} and Yingying Peng^{1,7,†}

¹*International Center for Quantum Materials, School of Physics, Peking University, Beijing 100871, China*

²*Beijing National Laboratory for Condensed Matter Physics,*

Institute of Physics, Chinese Academy of Sciences, Beijing 100190, China

³*Department of Physics, POSTECH, Pohang, Gyeongbuk, 37673, Republic of Korea*

⁴*Max Planck POSTECH/Korea Research Initiative,*

Center for Complex Phase Materials, Pohang, Gyeongbuk, 37673, Republic of Korea

⁵*PAL-XFEL, Pohang Accelerator Laboratory, POSTECH, Pohang, Gyeongbuk, 37673 Republic of Korea*

⁶*Photon Science Center, POSTECH, Pohang, Gyeongbuk, 37673 Republic of Korea*

⁷*Collaborative Innovation Center of Quantum Matter, Beijing 100871, China*

(Dated: June 10, 2025)

High-temperature superconductivity in cuprates remains one of the enduring puzzles of condensed matter physics, with charge order (CO) playing a central yet elusive role, particularly in the overdoped regime. Here, we employ time-resolved X-ray absorption spectroscopy and resonant X-ray scattering at a free-electron laser to probe the transient electronic density of states and ultrafast CO dynamics in overdoped $(\text{Bi,Pb})_{2.12}\text{Sr}_{1.88}\text{CuO}_{6+\delta}$. We reveal a striking pump laser wavelength dependence - the 800 nm light fails to suppress CO, whereas the 400 nm light effectively melts it. This behavior originates from the fact that 400 nm photons can promote electrons from the Zhang-Rice singlet band to the upper Hubbard band or apical oxygen states, while 800 nm photons lack the energy to excite electrons across the charge-transfer gap. The CO recovery time (~ 3 ps) matches that of the underdoped cuprates, indicating universal electronic instability in the phase diagram. Additionally, melting overdoped CO requires an order-of-magnitude higher fluence highlighting the role of lattice interactions. Our findings demonstrate orbital-selective photodoping and provide a route to ultrafast control of emergent quantum phases in correlated materials.

High-temperature superconductivity (SC) has been a central focus of condensed matter physics since its discovery [1–3], and understanding the mechanism of SC and what controls superconducting temperature (T_c) is a long-standing pursuit. Electronic correlations are pivotal in the formation of exotic phases intertwined with SC, and the electronic structure also significantly affects superconducting properties [1, 4–6]. Cuprate superconductors achieved by doping the charge-transfer insulators exhibit the highest T_c at ambient pressure and has potential applications in energy and quantum technology. The critical temperature is considered related to the charge transfer gap (CT gap), and various experimental and theoretical studies have demonstrated their anticorrelation [4–10]. Furthermore, complex electronic correlations in the CuO_2 plane usually lead to exotic phases intertwined with SC, such as charge order (CO), stripe order, and pseudogap phase.

Notable competitions between CO and SC have been observed in underdoped cuprate superconductors [11–16]. Furthermore, numerical calculations have found evidence for charge and/or spin density modulations as the ground state of the Hubbard model that competes with high-temperature SC [17, 18]. The overdoped

regime is usually considered as the Fermi-liquid state, which can be described by BCS theory. However, the lower than expected superfluid density, the formation of Cooper pairs well above T_c , and the ferromagnetic and nematic fluctuations provide evidence for unconventional SC behavior [19–24]. Surprisingly, resonant X-ray scattering experiments have detected CO in the overdoped $(\text{Bi,Pb})_{2.12}\text{Sr}_{1.88}\text{CuO}_6$ and heavily overdoped $\text{La}_{2-x}\text{Sr}_x\text{CuO}_4$ [25, 26]. Unlike its underdoped counterpart, overdoped CO remains nearly unchanged up to room temperature, raising the fundamental question whether overdoped CO shares the common origin as underdoped CO toward an ubiquitous instability. Elucidating the exotic states in the overdoped regime is crucial to understanding the evolution of T_c with hole doping and shedding light on the mechanism of high- T_c SC.

An emerging approach to exploring the CO mechanism is to investigate its dynamics in the time domain using ultrafast techniques. Femtosecond time-resolved optical and photoemission spectroscopy can provide insight into the roles of electron-electron and electron-phonon interactions through time- and fluence-dependent behaviors [28–32], yet these methods probe only the electronic structures rather than directly detecting CO. In recent years, time-resolved resonant X-ray scattering (tr-REXS) has enabled direct momentum-resolved measurements of the CO peak at Q_{CO} , offering a more direct probe of CO dynamics. Previous tr-REXS studies on underdoped

* These authors contributed equally to this work.

† yingying.peng@pku.edu.cn

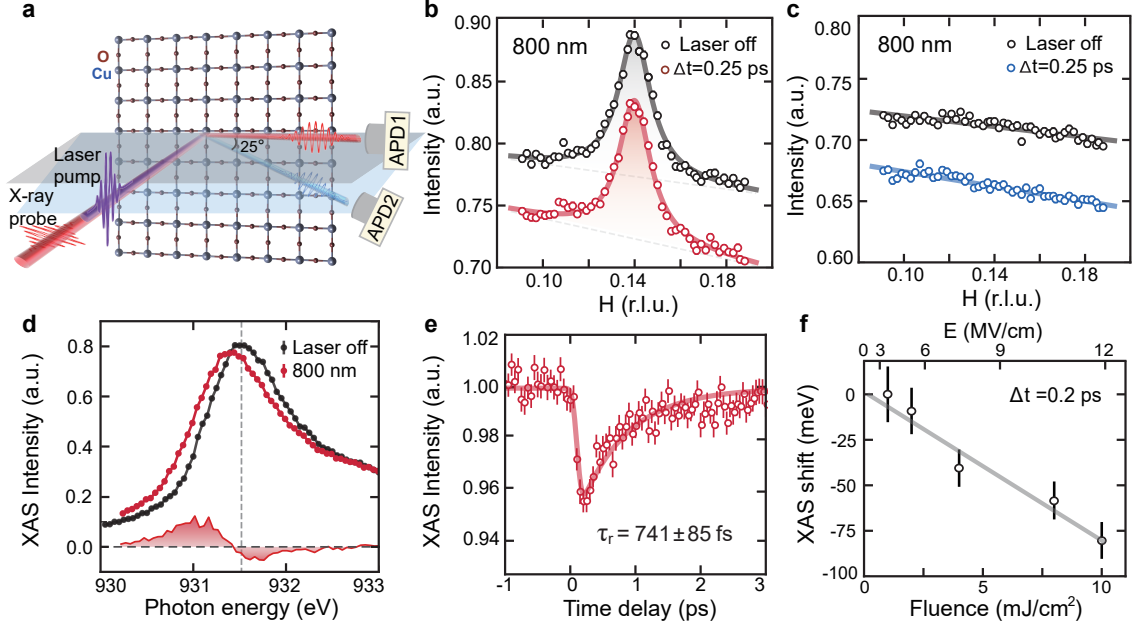


FIG. 1. **tr-REXS and tr-XAS in overdoped $(\text{Bi,Pb})_{2.12}\text{Sr}_{1.88}\text{CuO}_6$.** **a** Schematic experimental configuration. Optical laser pulses perturb the sample, and X-ray pulses probe the CO peak. Two detectors are used: APD1 is parallel to the scattering plane to detect the CO scattering signal, and APD2 is positioned at a 25-degree deviation off the scattering plane to detect the fluorescence signal. **b, c** Transverse momentum scan in the H direction through the CO peak before (black curve) and after excitation ($\Delta t = 0.25$ ps, red and blue curve), induced by an 800 nm pump with fluence of 5 mJ/cm^2 . The scattering signals **b** are fitted with the Lorentzian function and a linear background. The fluorescence signals **c** are fitted with a linear function. **d** XAS spectra in fluorescence-yield mode around Cu L_3 -edge before and after pump excitation ($\Delta t = 0.25$ ps) with fluence of 5 mJ/cm^2 . Three types of lines represent equilibrium (black), transient (red), and the corresponding difference spectrum. **e** Time dependence of XAS intensity at $\sim 931.5 \text{ eV}$ (dashed line in **d**), with 800 nm (3 mJ/cm^2) pumps. Intensities are normalized by the equilibrium absorption peak intensity. Error bars represent Poisson counting error. **f** XAS shift as a function of pump fluence. Experimental XAS shift values at the Cu L_3 -edge are obtained by fitting the XAS peak with a pseudo-Voigt function on a linear background, resembling [27]. The electric field is proportional to the square root of the laser fluence. The linear line is a guide to the eye. The error bars represent 1 standard deviation (s.d.) of the fit parameters.

cuprates reveal diffusive CO dynamics and the enhancement of CDW by suppressing SC with ultrafast laser pulses [15, 16, 33]. Studying how the CO melts and reconstructs in the overdoped regime and comparing it to that of underdoped cuprates can clarify the interactions in the formation and stabilization of the ordered phases.

Here, we employ time-resolved X-ray absorption spectroscopy (tr-XAS) to track light-induced changes in the electronic density of states, alongside time-resolved resonant soft X-ray scattering (tr-REXS) to probe CO dynamics in overdoped $(\text{Bi,Pb})_{2.12}\text{Sr}_{1.88}\text{CuO}_{6+\delta}$ (Bi2201 , $T_c = 11 \text{ K}$, $p \sim 0.21$). We observe a light-induced redistribution of the electronic density of states, consistent with an ultrafast renormalization of the on-site Coulomb interaction. Remarkably, the CO response shows a strong dependence on pump photon energy: 400 nm excitation melts the CO, while 800 nm light does not. This selective response reveals an orbital-dependent photodoping mechanism. We observe a CO recovery time of ~ 3 ps, comparable to that in underdoped cuprates, pointing to a universal electronic instability across the phase diagram. Furthermore, an order-of-magnitude

higher pump fluence is required to melt the CO in the overdoped regime, highlighting the important role of lattice coupling in stabilizing CO at high doping levels. Our results demonstrate that ultrafast optical pulses can selectively manipulate CO, offering a pathway to control quantum states in cuprates and other correlated materials.

RESULTS

Light-induced change in the electronic density of states

To probe electronic modulations associated with the overdoped CO, we tune the incident X-ray energy to around Cu L_3 -edge ($\sim 931.5 \text{ eV}$), and two avalanche photodiode detectors (APD1 and APD2) are utilized to detect the scattering signal and the fluorescence signal, respectively (Fig. 1a). We first use the 800 nm laser to pump the overdoped CO as previous studies demonstrate that laser pulses at 800 nm strongly perturb CO in underdoped cuprates. The CO peak is pronounced at the momentum transfer around the wave vector $\mathbf{Q}_{\text{CO}} = (0.14, 0, 3.5)$, consistent with previous equilibrium RIXS/REXS

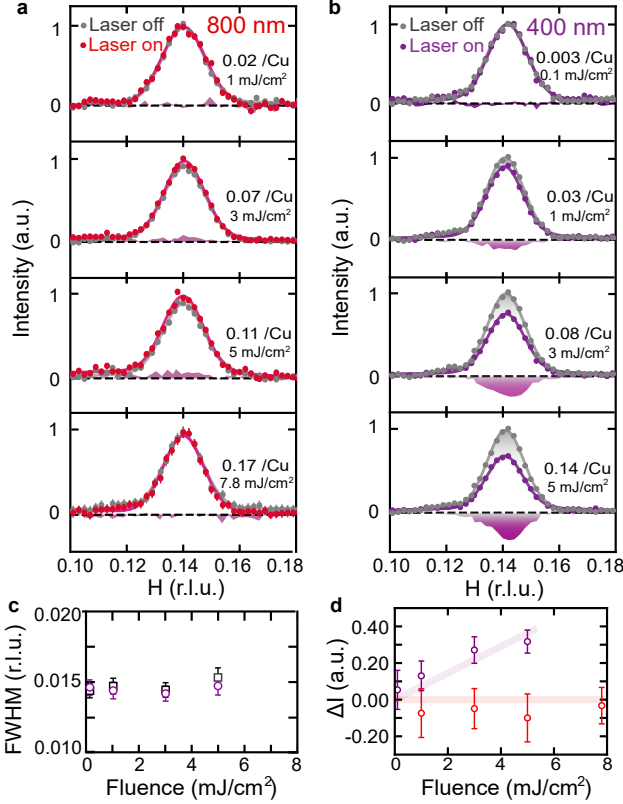


FIG. 2. **Pump-induced change in CO peak for the 800 nm and 400 nm pumps.** **a, b** The evolution of the CO scattering peak divided by the fluorescence signal with different laser fluences for the 800 nm **a** and 400 nm **b** pumps at $\Delta t = 0.25$ ps at 80 K. The purple shading indicates the difference between photo-induced states and equilibrium states. Solid lines are Lorentzian fits to the data with a linear background. **c** Fitted peak width (FWHM) of CO peaks before (black square) and after (purple circle) 400 nm excitation as a function of fluence. The error bars represent 1 standard deviation (s.d.) of the fit parameters. **d** Changes in CO intensity induced by 800 nm (red marker) and 400 nm (purple marker) pumps.

studies [25]. By applying the 800 nm laser pump, the intensities in the scattering signal and the fluorescence signal are both uniformly suppressed (see Fig. 1b, c). Meanwhile, the position and width of the CO peak do not change after photoexcitation. These photoinduced dynamics are in sharp contrast to the significant reduction in the intensity of the CO peak with unchanged background in underdoped cuprates [15, 16, 33].

To understand this intriguing non-equilibrium phenomenon in overdoped Bi2201, we trace the time-resolved XAS spectra at the Cu L_3 -edge to probe the local electronic structure. As shown in Fig. 1d, the absorption peak undergoes a significant redshift when comparing the equilibrium and transient spectra. The maximum energy of the transient XAS decreases by 80.3 ± 10.1 meV, leading to a uniform suppression of the scattering intensities as shown in Fig. 1b, c. Figure 1e displays the dynamics of the absorption peak intensity with an incident X-ray

at 931.5 eV (indicated by a dashed line in Fig. 1d). The evolution of the intensity induced by an 800 nm pump laser manifests itself as rapid decay after the pump (denoted “quenching”) and a subsequent recovery back to equilibrium. We use the following function to capture the relaxation:

$$I(t) = I_0 - \left[1 + \operatorname{erf}\left(\frac{t}{\tau_q}\right) \right] A_1 e^{-\frac{t}{\tau_r}}. \quad (1)$$

Here, I_0 represents the initial intensity normalized by the equilibrium scattering peak intensity, and τ_r represents the recovery time. The quench time is around 80 ± 22 fs limited by time resolution (~ 100 fs), and the recovery time is 741 ± 85 fs, consistent with the holon-doublon recombination dynamics in cuprates [27, 34–37]. Moreover, the XAS shift is found to increase nearly linearly with pump fluence within our measured range (Fig. 1f). The transient change of XAS also affects the Bragg peak intensity as shown in Supplementary Fig. 1. Previous time-resolved XAS studies on underdoped LBCO observed similar phenomena, where the laser electric field (~ 10 MV/cm) is considered strong enough to reduce Coulomb repulsion U due to dynamical enhancement of dielectric screening [27].

CO dynamics dependence on pump laser wavelength and fluence

To reveal whether the pump laser suppresses the CO intensity, we divide the scattering signal by the fluorescence signal, as shown in Fig. 2a (raw data are shown in Supplementary Fig. 3 and 4). We do not observe any CO suppression by the 800 nm pump up to 7.8 mJ/cm^2 . The corresponding photoexcited density per Cu is estimated to be 0.02, 0.07, 0.11, and 0.17 at fluence of 1, 3, 5 and 7.8 mJ/cm^2 , respectively (details are shown in Supplementary Fig. 5 and Note 3). In stark contrast, CO melts with increasing fluence when switching to the 400 nm pump (Fig. 2b). The CO peak intensity is unchanged at 0.1 mJ/cm^2 , which can easily melt the underdoped CO intensity [15, 16, 33]. This suggests that the overdoped CO is more robust to laser excitation than the underdoped CO, which agrees with its robust temperature behavior in the equilibrium state. We do not resolve any change in CO peak position and width (Fig. 2c), indicating that CO period and the correlation length remain unchanged in the photo-excited transient state. These indicate nonthermal behaviors as opposed to the peak broadening with increasing temperature [25], and different from the width broadening due to light-induced topological defects [38]. In addition, the width of Bragg peak (0, 0, 2) is almost unchanged after pumping (Supplementary Fig. 2), which also suggests the non-thermal effect. Figure 2d shows that the CO melting intensity increases with increasing fluence of 400 nm pump. On the other hand, the intensity change remains nearly zero under the 800 nm pump, even when the photons absorbed at each copper site are greater than those of the 400 nm pump

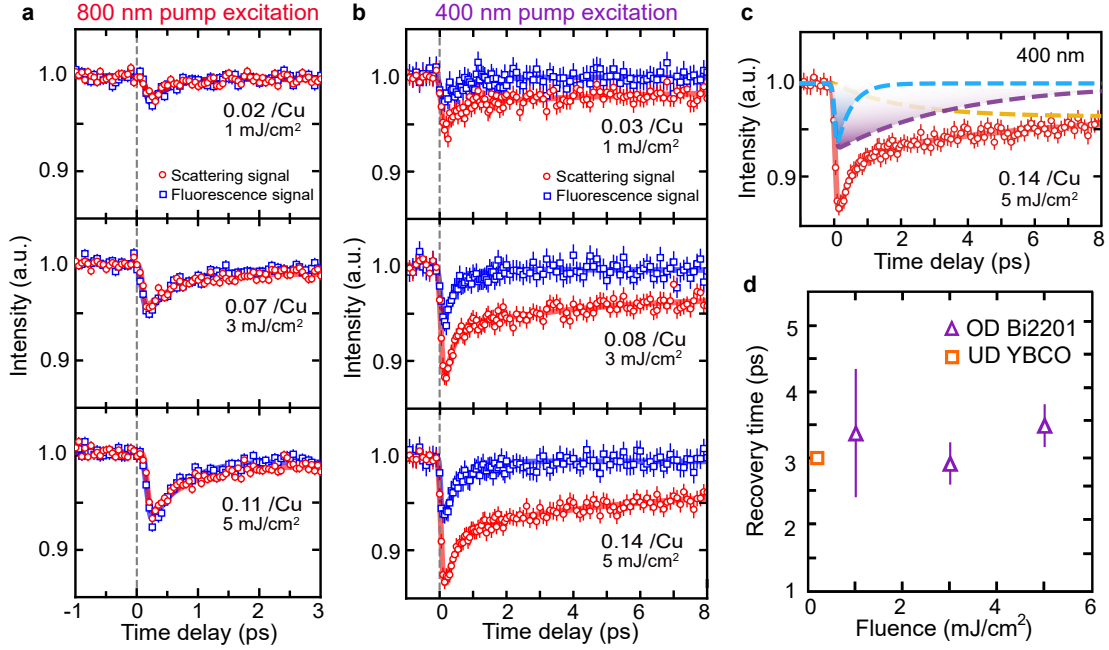


FIG. 3. **Fluence dependence of the dynamics at the CO peak.** **a, b** Evolution of the CO peak intensity induced by 800 nm **a** and 400 nm **b** pumps with various fluences. The red and blue curves correspond to scattering and fluorescence signals, respectively. These intensities are normalized by the equilibrium scattering intensity. **c** X-ray scattering signal measuring the CO dynamics with a pump fluence of 5 mJ/cm². The purple dashed line indicates a fit of the CO dynamics, and the blue dashed line indicates the electric dynamics. The orange dashed line represents the estimate of thermal heating effects. **d** Recovery time of CO dynamics as a function of fluence. The recovery time of CO on underdoped YBa₂Cu₃O_{6.67} (YBCO) at 0.16 mJ/cm² for an 800 nm pump is included [15]. The error bars represent 1 standard deviation (s.d.) of the fit parameters.

(compare Fig. 2a and b).

We then trace the dynamics at the peak position of CO (Q_{CO}) as the transient spectra are essential to distinguish ultrafast processes. As shown in Fig. 3a, the dynamics of the scattering and fluorescence signals collected by two APD detectors overlapped well with each other under the 800 nm pump excitation. We can use Eq. (1) to fit the dynamics. The intensity first undergoes a fast quench within a resolution-limited timescale ($\tau_q \sim 0.1$ ps), followed by a subpicosecond recovery timescale $\tau_r \sim 0.5$ ps, which increases slightly with increasing fluence. These electronic dynamics are equal to the transient XAS change in Fig. 1e. Moreover, we observed the same dynamics at a different momentum $Q=0.08$ r.l.u., which is away from Q_{CO} (Supplementary Fig. 6). These indicate that the time evolution of the intensity induced by the 800 nm pump arises from the photoinduced transient shift of XAS.

The CO dynamics at the 400 nm pump is notably different from that of the 800 nm pump. The scattering dynamics differs from the fluorescence dynamics, as shown in Fig. 3b. The fluorescence dynamics again originates from the photoinduced XAS shift for the 400 nm pump (Supplementary Fig. 1). However, the scattering signal under the 400 nm pump shows a higher quench percentage, where the melting intensity increases with increasing fluence. These require additional recovery processes. We

use the following function to fit the scattering dynamics induced by the 400 nm pump, which includes fast quenching, two recovery processes, and a thermal process.

$$I(t) = I_0 - \left[1 + \text{erf}\left(\frac{t}{\tau_q}\right) \right] \left[A_1 e^{-\frac{t}{\tau_{r1}}} + A_2 e^{-\frac{t}{\tau_{r2}}} \right] - A'(1 - e^{-\frac{t}{\tau'}}). \quad (2)$$

Here, τ_{r1} represents the fast recovery, τ_{r2} represents the slow recovery, and τ' denotes the lattice thermal timescale of ~ 2 ps [39, 40]. The decomposed processes are shown in Fig. 3c. The fast recovery process is ~ 0.5 ps as the fluorescence signals due to photoinduced electronic dynamics. Of particular interest is the slow recovery process ~ 3 ps that can be assigned to CO melting dynamics, which coincides with the recovery time of CO modulations in underdoped YBa₂Cu₃O_{6.67} and striped nickelate La_{1.75}Sr_{0.25}NiO₄ (Fig. 3d) [15, 16, 41]. These additional dynamics disappear at $Q=0.08$ r.l.u., when we move away from Q_{CO} (Supplementary Fig. 6). Therefore, the dynamics at the CO peak induced by the 400 nm pump originates from the combination of electronic dynamics and CO reconstruction in overdoped Bi2201.

DISCUSSION

The similar recovery timescales of CO in overdoped

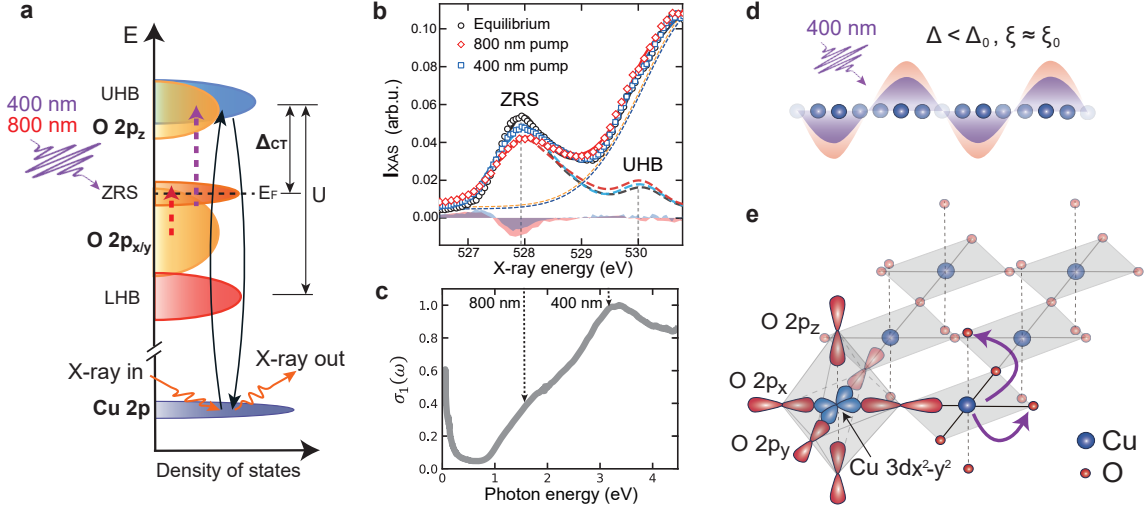


FIG. 4. **Dynamical response of charge order induced by the 800 nm and 400 nm pumps.** **a** Schematic plot of tr-REXS process in the hole-doped cuprates. LHB, lower Hubbard band; ZRS, Zhang-Rice singlet peak; UHB, upper Hubbard band; Δ_{CT} , charge transfer gap. The purple and red arrows correspond to the 400 and 800 nm pump respectively, while the orange and black arrows correspond to the X-ray probe process. **b** Time-resolved XAS spectra at O K absorption edges. The black curve indicates the equilibrium XAS spectrum, and the colored curves correspond to the transient XAS spectra at 0.25 ps after the 800 nm pump (red curve) and the 400 nm pump (blue curve) with fluence of 5 mJ/cm², corresponding to ~ 0.11 absorbed photons/Cu for the 800 nm pump and ~ 0.14 absorbed photons/Cu for the 400 nm pump. **c** Real part of the optical conductivity, $\sigma_1(\omega)$. **d** Schematic illustrating the dynamics of overdoped CO. The dashed grey line represents the equilibrium state of CO modulation. The solid purple line depicts the state excited by a 400 nm pump pulse. Δ and ξ denote CO amplitude and correlation length, respectively; Δ_0 and ξ_0 are values at equilibrium. Following photoexcitation, the CO amplitude is suppressed while the CO period and correlation length remain unchanged. **e** Sketch of the electron transfer process in the Cu-O octahedron of cuprates induced by the 400 nm pump.

Bi2201 with underdoped YBCO imply a common electronic instability in the cuprate phase diagram. By melting CO in the overdoped regime, where CO is unexpectedly robust [25, 26], the study hints at pathways to enhance transient SC, as seen in underdoped cuprates [42]. The excitation-energy dependence of the CO melting in overdoped Bi2201 provides fresh insight into understanding its microscopic origin. As illustrated schematically in Fig. 4a, the lower Hubbard band (LHB) and upper Hubbard band (UHB) arise from on-site Coulomb repulsion in the Cu 3d orbitals. Upon hole doping, the Zhang-Rice single (ZRS) band emerges because of hybridization between the hole on the planar Cu 3d orbital and the surrounding O 2p orbitals, forming the CT gap between the copper and oxygen states. Our O K-edge XAS spectra on Bi2201 reveal that the apical oxygen 2p_z band overlaps with UHB, and the CT gap (Δ_{CT}) is ~ 2 eV (Fig. 4b), consistent with previous optical and STM studies [6, 43–45]. Therefore, 400 nm (~ 3.1 eV) pumping can be effectively absorbed, as shown by the optical conductivity in Fig. 4c. It can induce the planar charge transfer from the ZRS band to the UHB band, or promote electrons from the Cu-O plane into apical oxygen states, as illustrated in Fig. 4e. This photoinduced charge transfer changes the in-plane doping level, which can suppress the CO amplitude without changing the period and correlation length (Fig. 4d). The out-of-plane electron

transfer is difficult to recover, consistent with our observed prolonged CO relaxation behavior that persists for up to 500 ps (Supplementary Fig. 7). Our observation aligns with theoretical predictions of orbitally selective photodoping in La_{1.885}Ba_{0.115}CuO₄, where photoexcitation redistributes holes from CuO₂ planes to charge reservoir layers, transiently increasing SC [46]. In contrast, although the 800 nm (~ 1.55 eV) photons exceed the metallic plasma edge (~ 1 eV) (Fig. 4c) and can excite electrons from the O 2p_{x/y} band to the empty ZRS band, it is less absorbed and does not induce CO suppression. Our tr-XAS measurements at the O K-edge (Fig. 4b) show that both 400 nm and 800 nm excitation suppress and broaden the ZRS peak due to photoinduced particle-hole excitations, consistent with prior observations in La_{1.905}Ba_{0.095}CuO₄ [27]. The weaker suppression at 400 nm reflects its tendency to deplete the ZRS band, whereas 800 nm excitation enhances occupancy by promoting electrons into it. Notably, the 800 nm laser already exceeds Δ_{CT} (~ 1.24 eV) in underdoped YBa₂Cu₃O_{6+x} and Δ_{CT} (~ 1.5 eV) in La_{2-x}Ba_xCuO₄ [15, 16, 33, 47–51], thus it can effectively melt CO in underdoped cuprates.

In underdoped cuprates and stripe-ordered nickelates, CO melting is commonly observed at relatively low excitation fluences of 0.01–1 mJ/cm², indicative of an underlying electronic instability [15, 16, 33, 41, 52]. The

excitation density used here is an order of magnitude higher. We notice that similar high fluence is required to melt COs in BaNi_2As_2 [53], CsV_3Sb_5 [54], and TaSe_2 and NbSe_2 [32], where electron-phonon coupling contributes significantly to CO formation. This resilience to laser fluence suggests that lattice interactions contribute importantly to the robustness of CO at high doping levels, consistent with the observed temperature stability of the CO [25, 26] and recent theoretical predictions [55]. To fully disentangle electronic and lattice contributions, future experiments utilizing phonon-resonant excitation, such as mid-infrared or THz-pump and X-ray-probe measurements, would be valuable. Such studies could reveal whether selectively driving specific phonon modes can suppress or enhance CO, as seen in the lattice-driven stripe dynamics of nickelates [56], thereby clarifying the interplay of charge, orbital and lattice degrees of freedom.

In summary, by combining time-resolved X-ray absorption spectroscopy and resonant X-ray scattering, we achieve momentum-resolved insights into non-equilibrium electronic structures in the overdoped cuprates. Our findings demonstrate that ultrafast, orbital-selective optical excitation provides a powerful approach to uncovering the intricate interplay between electronic and lattice degrees of freedom in CO dynamics. This approach offers a versatile framework for probing and controlling intertwined orders, such as charge, spin, and nematicity, across a broad class of quantum materials, including nickelates [57, 58], Kagome materials [59], and iron-based superconductors [60–62]. By tuning the pump-photon energy to match interband transitions involving different orbital characters, this methodology enables selective access to ultrafast dynamics, paving the way toward light-driven control of quantum phases and the design of functional quantum materials.

METHODS

Sample characterization

The single crystal of overdoped $(\text{Bi,Pb})_{2.12}\text{Sr}_{1.88}\text{CuO}_6$ was grown using the floating zone method of the traveling solvent. The method of sampling growth and characterization has previously been reported [63]. The single crystal used in this study has dimensions of about 2 mm by 2 mm by 0.2 mm. The lattice was defined by using the pseudo-tetragonal unit cell with $a = b = 3.83 \text{ \AA}$ and $c = 24.54 \text{ \AA}$. The sample was cleaved and examined by X-ray diffraction measurements (XRD) before experiments to confirm its highly crystalline quality. Single crystal X-ray diffraction measurements were performed using the custom-designed X-ray instrument equipped with a Xenocs Genix3D Mo $K\alpha$ (17.48 keV) X-ray source, which provides $\sim 2.5 \times 10^7$ photons/sec in a beam spot size of $150 \mu\text{m}$ at sample position [64]. The T_c value ($\sim 11 \text{ K}$) of overdoped Bi2201 is defined at the onset temperature of the diamagnetism by magnetic

measurement, performed with a 1 Oe magnetic field applied along the c-axis using a SQUID magnetometer (MPMS XL1, Quantum Design), which shows a sharp transition width of approximately 1 K.

tr-RSXS measurements

The tr-RSXS experiments were carried out at the SSS-RSXS endstation of PAL-XFEL [65]. The sample was mounted on a six-axis open-circle cryostat manipulator and measured at a base temperature of $\sim 80 \text{ K}$ using liquid nitrogen. The sample surface was perpendicular to the crystalline c axis and the horizontal scattering plane was parallel to the bc plane. X-ray pulses with pulse duration $\sim 80 \text{ fs}$ and 60 Hz repetition rate were used for the soft X-ray probe. The X-ray was linear horizontal polarized (π -polarization), and the photon energy was tuned to Cu L_3 -edge (931.5 eV). To trace CO, we fixed the scattering angle of the detector at $2\theta = 163^\circ$. For Q_{CO} (H) $\sim 0.14 \text{ r.l.u.}$, the L value corresponds to 3.5 r.l.u.

We utilized a Ti:sapphire laser to provide optical lasers at 1.55 eV (800 nm) and 3.1 eV (400 nm) with a pulse duration of $\sim 50 \text{ fs}$ and a repetition rate of 30 Hz. The 800 nm is converted to 400 nm through the BBO crystal. The overall time resolution was $\sim 107 \text{ fs}$, determined by measuring the pump-probe cross-correlation. The optical laser was nearly parallel to the incident X-ray beam, with an angle difference of less than 1° . The pump fluence ranged from 0.1 to 10 mJ/cm^2 was mainly used. The size of the X-ray spot in the sample position was $\sim 160 (H) \times 240 (V) \mu\text{m}^2$ (FWHM), while the diameter of the optical laser spot diameter was about $700 \mu\text{m}$ for 800 nm and $400 \mu\text{m}$ for 400 nm in FWHM. The X-ray repetition rate was twice that of the pump pulses, enabling comparison of diffraction signals before and after pump excitation.

Optical measurements

The optical conductivity data were obtained from the reflectivity spectra $R(\omega)$ at room temperature and under ambient conditions. The near-normal incidence ab-plane reflectivity $R(\omega)$ in the frequency range of 0.05 to 2.5 eV was measured using a Bruker Vertex 80V Fourier transform infrared (FTIR) spectrometer. In the higher frequency range of 2.5 to 5 eV, $R(\omega)$ was measured using a halogen and deuterium lamp as the light source and detected by a high-sensitivity NOVA spectrometer (Idea Optics, China). For the low-frequency extrapolation ($< 0.05 \text{ eV}$), the Hagen-Rubens relation was used. The real part of the optical conductivity, $\sigma_1(\omega)$, was obtained from the measured reflectivity via Kramers-Kronig transformation for OD Bi2201.

Data availability: All data needed to evaluate the conclusions in the paper are present in the paper and/or the Supplementary Materials. The data are available from the corresponding author upon request.

-
- [1] Zhou, X. *et al.* High-temperature superconductivity. *Nat. Rev. Phys.* **3**, 462–465 (2021).
- [2] Keimer, B., Kivelson, S. A., Norman, M. R., Uchida, S. & Zaanen, J. From quantum matter to high-temperature superconductivity in copper oxides. *Nature* **518**, 179–186 (2015).
- [3] Paglionee, J. & Greene, R. L. High-temperature superconductivity in iron-based materials. *Nat. Phys.* **6**, 645–658 (2010).
- [4] Wang, Z. *et al.* Correlating the charge-transfer gap to the maximum transition temperature in $\text{Bi}_2\text{Sr}_2\text{Ca}_{n-1}\text{Cu}_n\text{O}_{2n+4+\delta}$. *Science* **381**, 227–231 (2023).
- [5] Ruan, W. *et al.* Relationship between the parent charge transfer gap and maximum transition temperature in cuprates. *Sci. Bull.* **61**, 1826–1832 (2016).
- [6] Peli, S. *et al.* Mottness at finite doping and charge instabilities in cuprates. *Nat. Phys.* **13**, 806–811 (2017).
- [7] Zou, C. *et al.* Particle-hole asymmetric superconducting coherence peaks in overdoped cuprates. *Nat. Phys.* **18**, 551–557 (2022).
- [8] Schneider, M. *et al.* Evolution of the density of states at the fermi level of $\text{Bi}_{2-y}\text{Pb}_y\text{Sr}_{2-x}\text{La}_x\text{CuO}_{6+\delta}$ and $\text{Bi}_2\text{Sr}_{2-x}\text{La}_x\text{CuO}_{6+\delta}$ cuprates with hole doping. *Phys. Rev. B* **72**, 014504 (2005).
- [9] Cui, Z.-H. *et al.* Ground-state phase diagram of the three-band hubbard model from density matrix embedding theory. *Phys. Rev. Res.* **2**, 043259 (2020).
- [10] Chakravarty, S., Kee, H.-Y. & Völker, K. An explanation for a universality of transition temperatures in families of copper oxide superconductors. *Nature* **428**, 53–55 (2004).
- [11] Chang, J. *et al.* Direct observation of competition between superconductivity and charge density wave order in $\text{YBa}_2\text{Cu}_3\text{O}_{6.67}$. *Nat. Phys.* **8**, 871–876 (2012).
- [12] da Silva Neto, E. H. *et al.* Ubiquitous interplay between charge ordering and high-temperature superconductivity in cuprates. *Science* **343**, 393–396 (2014).
- [13] Ghiringhelli, G. *et al.* Long-range incommensurate charge fluctuations in $(\text{Y,Nd})\text{Ba}_2\text{Cu}_3\text{O}_{6+x}$. *Science* **337**, 821–825 (2012).
- [14] Lee, W.-S. *et al.* Spectroscopic fingerprint of charge order melting driven by quantum fluctuations in a cuprate. *Nat. Phys.* **17**, 53–57 (2021).
- [15] Smallwood, C. L., Hinton, J. P., Jozwiak, C. *et al.* Enhanced charge density wave coherence in a light-quenched, high-temperature superconductor. *Science* **376**, 860–864 (2022).
- [16] Hoyoung, J., Sanghoon, S., Takumi, K. *et al.* Characterization of photoinduced normal state through charge density wave in superconducting $\text{YBa}_2\text{Cu}_3\text{O}_{6.67}$. *Sci. Adv.* **8**, eabk0832 (2022).
- [17] Zheng, B.-X. *et al.* Stripe order in the underdoped region of the two-dimensional Hubbard model. *Science* **358**, 1155–1160 (2017).
- [18] Jiang, H.-C. & Devereaux, T. P. Superconductivity in the doped Hubbard model and its interplay with next-nearest hopping t' . *Science* **365**, 1424–1428 (2019).
- [19] Božović, I., He, X., Wu, J. & Bollinger, A. Dependence of the critical temperature in overdoped copper oxides on superfluid density. *Nature* **536**, 309–311 (2016).
- [20] Uemura, Y. *et al.* Magnetic-field penetration depth in $\text{Ti}_2\text{Ba}_2\text{CuO}_{6+\delta}$ in the overdoped regime. *Nature* **364**, 605–607 (1993).
- [21] He, Y. *et al.* Superconducting fluctuations in overdoped $\text{Bi}_2\text{Sr}_2\text{CaCu}_2\text{O}_{8+\delta}$. *Phys. Rev. X* **11**, 031068 (2021).
- [22] Kondo, T. *et al.* Point nodes persisting far beyond T_C in bi2212 . *Nat. commun.* **6**, 7699 (2015).
- [23] Kurashima, K. *et al.* Development of ferromagnetic fluctuations in heavily overdoped $(\text{Bi, Pb})_2\text{Sr}_2\text{CuO}_{6+\delta}$ copper oxides. *Phys. Rev. Lett.* **121**, 057002 (2018).
- [24] Ayres, J. *et al.* Incoherent transport across the strange-metal regime of overdoped cuprates. *Nature* **595**, 661–666 (2021).
- [25] Peng, Y., Fumagalli, R., Ding, Y. *et al.* Re-entrant charge order in overdoped $(\text{Bi,Pb})_{2.12}\text{Sr}_{1.88}\text{CuO}_{6+\delta}$ outside the pseudogap regime. *Nat. Mater.* **17**, 697–702 (2018).
- [26] Li, Q. *et al.* Prevailing charge order in overdoped $\text{La}_{2-x}\text{Sr}_x\text{CuO}_4$ beyond the superconducting dome. *Phys. Rev. Lett.* **131**, 116002 (2023).
- [27] Baykuseva, D. R. *et al.* Ultrafast renormalization of the on-site coulomb repulsion in a cuprate superconductor. *Phys. Rev. X* **12**, 011013 (2022).
- [28] Tomeljak, A. *et al.* Dynamics of photoinduced charge-density-wave to metal phase transition in $\text{K}_{0.3}\text{MoO}_3$. *Phys. Rev. Lett.* **102**, 066404 (2009).
- [29] Hellmann, S. *et al.* Ultrafast melting of a charge-density wave in the Mott insulator 1T-TaS_2 . *Phys. Rev. Lett.* **105**, 187401 (2010).
- [30] Hellmann, S. *et al.* Time-domain classification of charge-density-wave insulators. *Nat. Commun.* **3**, 1069 (2012).
- [31] Schmitt, F. *et al.* Transient electronic structure and melting of a charge density wave in TbTe_3 . *Science* **321**, 1649–1652 (2008).
- [32] Nakata, Y. *et al.* Robust charge-density wave strengthened by electron correlations in monolayer 1T-TaSe_2 and 1T-NbSe_2 . *Nat. commun.* **12**, 5873 (2021).
- [33] Matteo, M., Sangjun, L., Ali, A., H. *et al.* Ultrafast time-resolved x-ray scattering reveals diffusive charge order dynamics in $\text{La}_{2-x}\text{Ba}_x\text{CuO}_4$. *Sci. Adv.* **5**, eaax3346 (2019).
- [34] Lenarcic, Z. & Prelovsek, P. Ultrafast charge recombination in a photoexcited Mott-Hubbard insulator. *Phys. Rev. Lett.* **111**, 016401 (2013).
- [35] Wall, S., Brida, D., Clark, S. *et al.* Quantum interference between charge excitation paths in a solid-state Mott insulator. *Nat. Phys.* **7**, 114–118 (2011).
- [36] Strohmaier, N. *et al.* Observation of elastic doublon decay in the fermi-hubbard model. *Phys. Rev. Lett.* **104**, 080401 (2010).
- [37] Okamoto, H. *et al.* Photoinduced transition from Mott insulator to metal in the undoped cuprates Nd_2CuO_4 and La_2CuO_4 . *Phys. Rev. B* **83**, 125102 (2011).
- [38] Zong, A. *et al.* Evidence for topological defects in a photoinduced phase transition. *Nat. Phys.* **15**, 27–31 (2019).
- [39] Giannetti, C. *et al.* Ultrafast optical spectroscopy of strongly correlated materials and high-temperature superconductors: a non-equilibrium approach. *Adv. Phys.* **65**, 58–238 (2016).
- [40] Perfetti, L. *et al.* Ultrafast electron relaxation in superconducting $\text{Bi}_2\text{Sr}_2\text{CaCu}_2\text{O}_{8+\delta}$ by time-resolved photoelectron spectroscopy. *Phys. Rev. Lett.* **99**, 197001 (2007).
- [41] Lee, W.-S. *et al.* Phase fluctuations and the absence

- of topological defects in a photo-excited charge-ordered nickelate. *Nat. commun.* **3**, 838 (2012).
- [42] Fausti, D. *et al.* Light-induced superconductivity in a stripe-ordered cuprate. *Science* **331**, 189–191 (2011).
- [43] Van Heumen, E., Meevasana, W., Kuzmenko, A., Eisaki, H. & Van Der Marel, D. Doping-dependent optical properties of Bi2201. *New J. Phys.* **11**, 055067 (2009).
- [44] Cai, P. *et al.* Visualizing the evolution from the Mott insulator to a charge-ordered insulator in lightly doped cuprates. *Nat. Phys.* **12**, 1047–1051 (2016).
- [45] Giannetti, C. *et al.* Revealing the high-energy electronic excitations underlying the onset of high-temperature superconductivity in cuprates. *Nat. Commun.* **2**, 353 (2011).
- [46] Tang, T., Wang, Y., Moritz, B. & Devereaux, T. P. Orbital selective resonant photodoping to enhance superconductivity. *Phys. Rev. B* **104**, 174516 (2021).
- [47] Lee, Y. *et al.* Electrodynamics of the nodal metal state in weakly doped high- T_c cuprates. *Phys. Rev. B* **72**, 054529 (2005).
- [48] Achkar, A. *et al.* Orbital symmetry of charge-density-wave order in $\text{La}_{1.875}\text{Ba}_{0.125}\text{CuO}_4$ and $\text{YBa}_2\text{Cu}_3\text{O}_{6.67}$. *Nat. Mater.* **15**, 616–620 (2016).
- [49] Lenarčič, Z. & Prelovšek, P. Charge recombination in undoped cuprates. *Phys. Rev. B* **90**, 235136 (2014).
- [50] Golež, D., Boehnke, L., Eckstein, M. & Werner, P. Dynamics of photodoped charge transfer insulators. *Phys. Rev. B* **100**, 041111 (2019).
- [51] Okamoto, H. *et al.* Photoinduced transition from Mott insulator to metal in the undoped cuprates Nd_2CuO_4 and La_2CuO_4 . *Phys. Rev. B* **83**, 125102 (2011).
- [52] Chuang, Y. *et al.* Real-time manifestation of strongly coupled spin and charge order parameters in stripe-ordered $\text{La}_{1.75}\text{Sr}_{0.25}\text{NiO}_4$ nickelate crystals using time-resolved resonant x-ray diffraction. *Phys. Rev. Lett.* **110**, 127404 (2013).
- [53] Pokharel, A. R. *et al.* Dynamics of collective modes in an unconventional charge density wave system BaNi_2As_2 . *Commun. Phys.* **5**, 141 (2022).
- [54] Ning, H. *et al.* Dynamical decoding of the competition between charge density waves in a kagome superconductor. *Nat. Commun.* **15**, 7286 (2024).
- [55] Liu, J., Li, S., Huang, E. W. & Wang, Y. Charge density wave state in extremely overdoped cuprates driven by phonons. *Phys. Rev. B* **110**, 115133 (2024).
- [56] Lee, W. *et al.* Nonequilibrium lattice-driven dynamics of stripes in nickelates using time-resolved x-ray scattering. *Phys. Rev. B* **95**, 121105 (2017).
- [57] Zhang, M. *et al.* Spin-density wave and superconductivity in $\text{La}_4\text{Ni}_3\text{O}_{10}$ under ambient pressure. *Phys. Rev. B* **111**, 144502 (2025).
- [58] Yi, X.-W. *et al.* Nature of charge density waves and metal-insulator transition in pressurized $\text{La}_3\text{Ni}_2\text{O}_7$. *Phys. Rev. B* **110**, L140508 (2024).
- [59] Huang, Z. *et al.* Revealing the orbital origins of exotic electronic states with Ti substitution in kagome superconductor CsV_3Sb_5 . *Phys. Rev. Lett.* **134**, 056001 (2025).
- [60] Sprau, P. O. *et al.* Discovery of orbital-selective cooper pairing in FeSe. *Science* **357**, 75–80 (2017).
- [61] Böhmer, A. E., Chu, J.-H., Lederer, S. & Yi, M. Nematicity and nematic fluctuations in iron-based superconductors. *Nat. Phys.* **18**, 1412–1419 (2022).
- [62] Yi, M., Zhang, Y., Shen, Z.-X. & Lu, D. Role of the orbital degree of freedom in iron-based superconductors. *npj Quantum Mater.* **2**, 57 (2017).
- [63] Lin, Z. *et al.* High-quality large-sized single crystals of pb-doped $\text{Bi}_2\text{Sr}_2\text{CuO}_{6+\delta}$ high- T_c superconductors grown with traveling solvent floating zone method. *Chinese Phys. Lett.* **27**, 087401 (2010).
- [64] Xiao, Q. *et al.* Coexistence of multiple stacking charge density waves in kagome superconductor CsV_3Sb_5 . *Phys. Rev. Res.* **5**, L012032 (2023).
- [65] Jang, H. *et al.* Time-resolved resonant elastic soft x-ray scattering at Pohang Accelerator Laboratory x-ray free electron laser. *Rev. Sci. Instrum.* **91**, 083904 (2020).

Acknowledgements: The tr-RSXS experiments were performed using the RSXS instrument at PAL-XFEL (Proposal No. 2022-2nd-SSS-002) funded by the Ministry of Science and ICT of Korea. We acknowledge the valuable discussion with Yao Wang, Giacomo Ghiringhelli, Thomas P. Devereaux, Brian Moritz, Yuan Li, and Simon E. Wall. Y.Y.P. is grateful for financial support from the Ministry of Science and Technology of China (Grants No. 2024YFA1408702 and No. 2021YFA1401903) and the National Natural Science Foundation of China (Grant No. 12374143). X.J.Z.'s work is supported by the National Natural Science Foundation of China (Grant No. 12488201) and the National Key Research and Development Program of China (Grant No. 2021YFA1401800). N.L.W. acknowledges the support by the National Natural Science Foundation of China (Grant No. 12488201). B.L. and H.J. acknowledge the support by the National Research Foundation grant funded by the Korea government (MSIT) (Grant No. RS-2022-NR068223).

Author contributions: X.J. and Y.P. proposed and designed the research. X.J., Q.L., Q.Q., B.L., H.C., H.J. and Y.P. carried out the tr-RSXS experiments. L.Y., J.H., T.D. and N.W. carried out the optical experiments. Y.C. and X.Z. provided the OD-Bi2201 single crystals. X.J. characterized the samples. X.J. and Y.P. analyzed the data and prepared the manuscript. All authors have read and approved the final version of the manuscript.

Competing interests: The authors declare that they have no competing interests.

SUPPLEMENTARY NOTES

Note 1. Time-resolved X-ray absorption spectra and Bragg peak dynamics

We trace the time-resolved X-ray absorption spectra in overdoped $(\text{Bi,Pb})_{2.12}\text{Sr}_{1.88}\text{CuO}_{6+\delta}$ triggered by intense near-infrared pump pulses (800 and 400 nm), as shown in Supplementary Fig. 1a. By comparing equilibrium and transient XAS spectra, we observe substantial photo-induced redshift at the Cu L_3 edge. The photoinduced shift of the UHB peak ($\sim 80.3 \pm 10.1$ meV) are similar at 400 nm and 800 nm lasers with the same fluence of 5 mJ/cm^2 . Supplementary Fig. 1b shows the dynamics at the absorption peak (indicated by the vertical line) for the 800 and 400 nm pumps, which is similar to the photoinduced XAS shift in $\text{La}_{1.905}\text{Ba}_{0.095}\text{CuO}_4$ [27]. Using Eq.(1) in the main text to fit the dynamics, the recovery time is around 741 ± 85 fs with 800 nm laser and 755 ± 84 fs with 400 nm laser. These timescales are consistent with holon-doublon recombination dynamics in other cuprates [34–37]. We also trace the profile of Bragg peak (0, 0, 2) before and after excitation at two different X-ray energies, as shown in Supplementary Fig. 2. The widths are nearly unchanged, implying a nonthermal effect. The intensity of the Bragg peak collected at 932 eV (on the right side of the resonant absorption peak) is suppressed (Supplementary Fig. 2a), and the recovery time of the corresponding dynamics is ~ 430 fs (Supplementary Fig. 2c). In contrast, the intensity of the Bragg peak collected at 931 eV (on the left side of the resonant absorption peak) is enhanced (Supplementary Fig. 2b), with the corresponding recovery time of ~ 300 fs (Supplementary Fig. 2d).

Note 2. Raw data of transient CO profile at different fluences

We tune the X-ray energy to the Cu L_3 -edge (~ 931.5 eV) to probe the CO profile at the delay time of 0.25 ps. The raw data for the 800 nm pump at fluences of 1, 3, 5 and 7.8 mJ/cm^2 are shown in Supplementary Fig. 3. The scattering intensity is uniformly suppressed with increasing fluences (Supplementary Fig. 3a), while the width of the CO peak remains unchanged after pump excitation. Alongside this, the fluorescence signal is also uniformly suppressed (Supplementary Fig. 3b).

The raw data for 400 nm pump at different fluences are shown in Supplementary Fig. 4. When using a 0.1 mJ/cm^2 pump laser, the CO peak profile is almost unchanged after excitation, indicating that overdoped CO is more resistant to laser excitation than CO in underdoped cuprates and stripe-ordered nickelates [15, 16, 33, 41, 52]. In contrast to the 800 nm pump, the suppression of the CO profile induced by the 400 nm pump is not uniform - the suppression is more pronounced at the CO peak position than away from the CO peak. Yet, the fluorescence signal is

uniformly suppressed at 400 nm similar to 800 nm (see Supplementary Fig. 4b).

Note 3. Calculation of laser photoexcited density

In order to directly compare the effect of different pumps excitations on the sample, we derive the laser photoexcited density per copper site according to the laser fluence. First of all, we calculate the number of absorbed photons,

$$N_{\text{abs}} = \frac{(1 - R)(1 - e^{-1})F}{\lambda_p \hbar \omega_p}. \quad (\text{S3})$$

where N_{abs} indicates the number of absorbed photons per unit volume, R indicates the reflectivity of $(\text{Bi,Pb})_{2.12}\text{Sr}_{1.88}\text{CuO}_{6+\delta}$, F corresponds to the laser fluence, λ_p is the penetration depth of the pump laser, and $\hbar \omega_p$ is the energy of each pump photon. We obtain the values of R and λ_p by optical measurements, as shown in Supplementary Fig. 5a. For the 800 nm pump, $R \sim 0.13$; for the 400 nm pump, $R \sim 0.17$. Since laser penetration depth = laser wavelength / $(2\pi \cdot k)$, we can calculate the penetration depth based on the absorption index (k) through optical measurements, as shown in Supplementary Fig. 5b. For the 800 nm pump, $k \sim 0.72$, the penetration depth is about 180 nm; for the 400 nm pump, $k \sim 0.94$, the penetration depth is about 70 nm. Notably, the penetration depth of both lasers is greater than that of the X-rays at Cu L_3 -edge. Then, since the volume of each Cu^{2+} in overdoped Bi2201 is on the order of 10^{-22} cm^3 , the excitation density per Cu^{2+} is equal to $N_{\text{abs}}/V_{\text{Cu}^{2+}}$. Therefore, for the 800 nm pump with laser fluences of 1, 3, 5 and 7.8 mJ/cm^2 , the corresponding laser photoexcited densities per copper site are 0.02, 0.07, 0.11 and 0.17 absorbed photons/Cu, respectively. For the 400 nm pump with laser fluences of 0.1, 1, 3 and 5 mJ/cm^2 , the corresponding laser photoexcited densities per copper site are 0.003, 0.03, 0.08 and 0.14 absorbed photons/Cu, respectively.

In addition, the absorptivity of overdoped Bi2201 at 800 nm and 400 nm lasers is relatively similar (Supplementary Fig. 5b), demonstrating that the different CO melting phenomena cannot be attributed to the difference in absorption.

Note 4. Momentum dependence of scattering dynamics for the 800 and 400 nm pumps

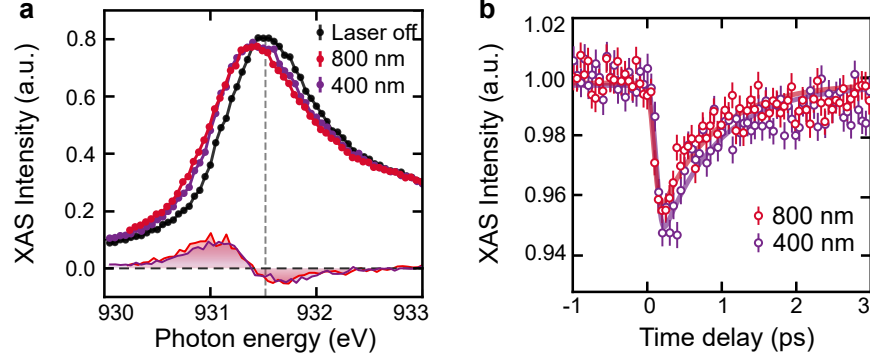
Supplementary Fig. 6a and b demonstrate the scattering dynamics at and away from Q_{CO} ($Q=0.14$ and 0.08 r.l.u., respectively) for the 800 and 400 nm pumps. The dynamics at Q_{CO} and away from Q_{CO} are similar at the 800 nm pump (Supplementary Fig. 6a), which is due to photoinduced XAS shift. In contrast to the 800 nm pump, the dynamics at two different momenta are different at the 400 nm pump (Supplementary Fig. 6b). These momentum-dependent dynamics imply the combination of electron and CO dynamics induced

by the 400 nm pump at Q_{CO} .

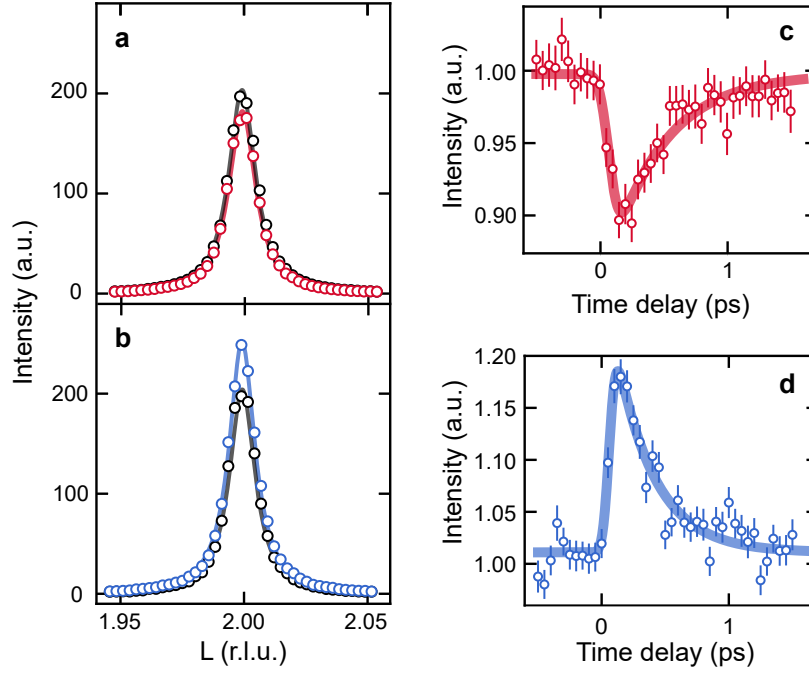
Note 5. Long-time scan of CO dynamics induced by the 400 nm pump

We measure the change in intensity of the scattering peak over a time scale of up to 500 ps, as shown in Supplementary Fig. 7. At 9 ps after 400 nm excitation, the intensity recovers up to 98% of the equilibrium value. Subsequently, up to 500 ps, the intensity recovers rather slowly to nearly 0.99, but still not to the equilibrium value. This is consistent with the relaxation of the out-of-plane electron transfer required for a long time.

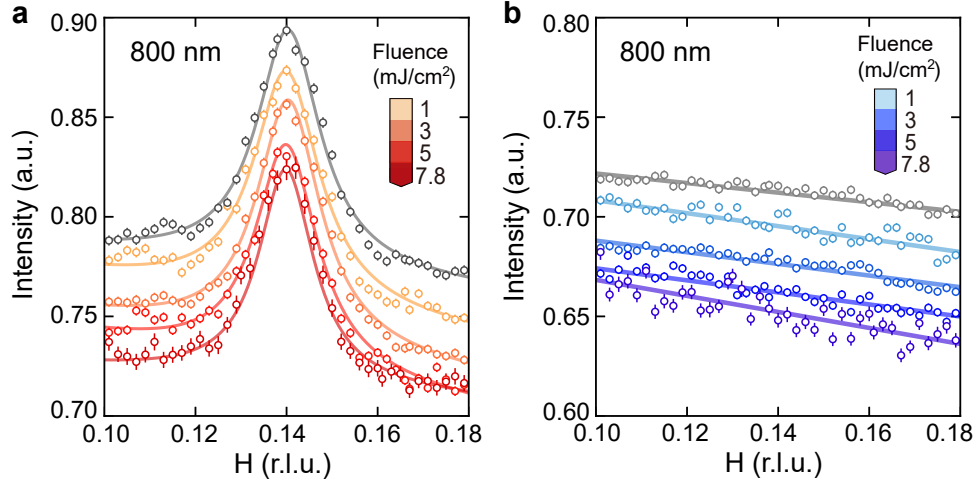
SUPPLEMENTARY FIGURES



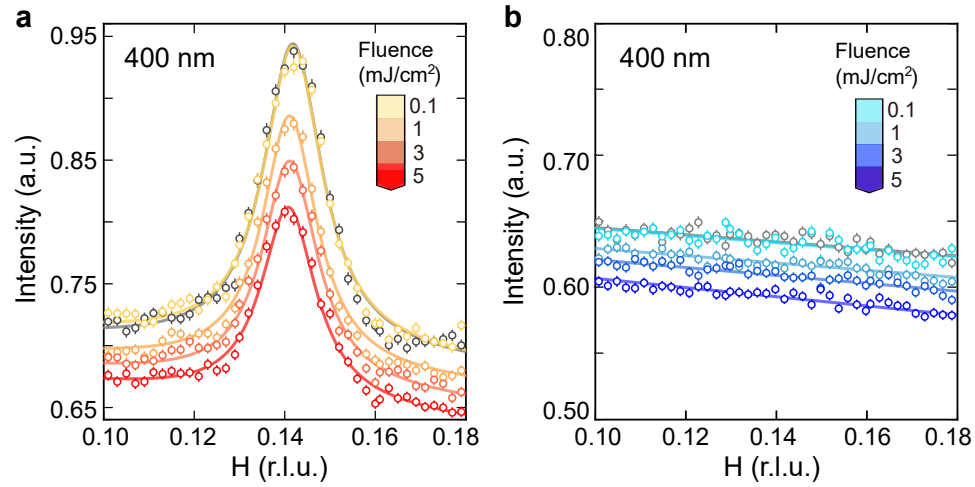
Supplementary Figure 1. **Pump-induced X-ray absorption and electronic dynamics.** **a** XAS spectra in fluorescence-yield mode before and after pump excitation ($\Delta t \sim 0.25$ ps, fluence = 5 mJ/cm^2 , corresponding to ~ 0.11 absorbed photons/Cu for the 800 nm pump and ~ 0.14 absorbed photons/Cu for the 400 nm pump) arrival at Cu L_3 -edge. Three types of lines represent equilibrium (black), transient (red for the 800 nm pump and purple for the 400 nm pump), and difference spectrum (shading). The equilibrium absorption peak is marked by dashed lines, which is found to shift after excitation. **b** The time evolution of the absorption peak at ~ 931.5 eV, with excitation of 800 nm (3 mJ/cm^2 , ~ 0.07 absorbed photons/Cu) and 400 nm (5 mJ/cm^2 , ~ 0.14 absorbed photons/Cu), respectively. Intensities are normalized by the equilibrium absorption peak intensity.



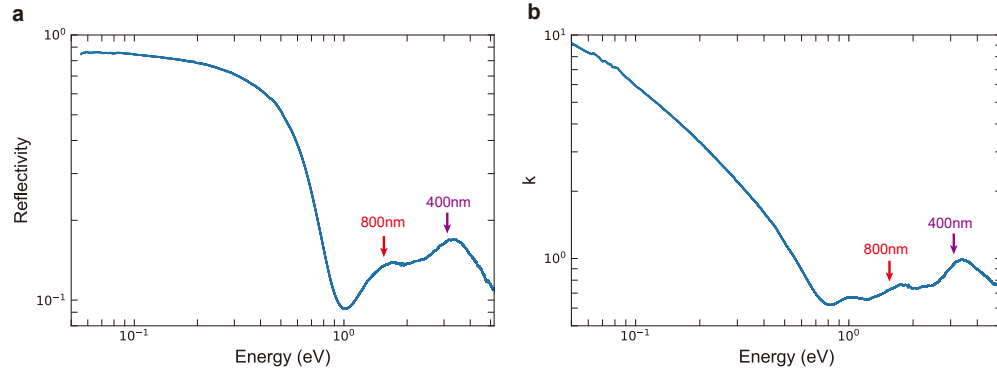
Supplementary Figure 2. **Dynamics of Bragg peak (0, 0, 2) at different X-ray energies.** **a** Bragg peak (0, 0, 2) without pump and $\Delta t = 0.25$ ps after the 800 pump with fluence of 5 mJ/cm^2 , with X-ray of 932 eV (on the right side of the resonant absorption peak at 931.5 eV). Solid lines are Lorentzian fits to the data. **b** Bragg peak (0, 0, 2) without pump and $\Delta t = 0.15$ ps after the 800 pump with fluence of 5 mJ/cm^2 , with X-ray of 931 eV (on the left side of the resonant absorption peak at 931.5 eV). Solid lines are Lorentzian fits to the data. **c, d** Evolution of the Bragg peak with X-ray of 932 eV **c** and 931 eV **d**. Dynamics are fitted with Eq.(1) in the main text.



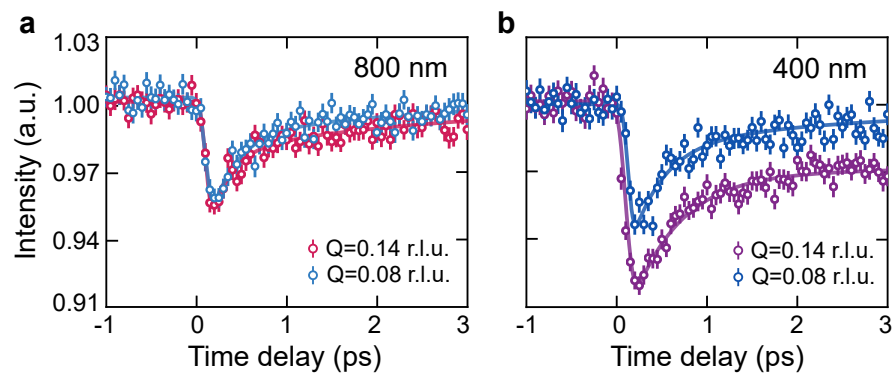
Supplementary Figure 3. **Transient CO profile and fluorescence signal at 800 nm pump.** **a, b** The CO profile **a** and fluorescence signal **b** without pump (grey markers) and after pump excitation (0.25 ps, 800 nm) with fluence of 1, 3, 5 and 7.8 mJ/cm² (color markers). Solid lines are fit using the Lorentzian function and a linear background. Error bars represent Poisson counting error.



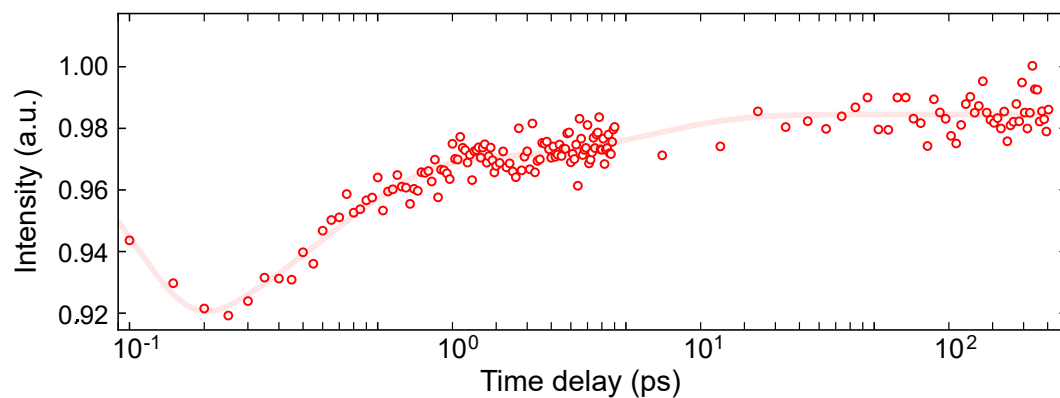
Supplementary Figure 4. **Transient CO profile and fluorescence signal at 400 nm pump.** **a, b** The CO profile **a** and fluorescence signal **b** without pump (grey markers) and after pump excitation (0.25 ps, 400 nm) with fluence of 0.1, 1, 3 and 5 mJ/cm² (color markers). Solid lines are fit using the Lorentzian function and a linear background.



Supplementary Figure 5. **Equilibrium optical measurements of overdoped $(\text{Bi,Pb})_{2.12}\text{Sr}_{1.88}\text{CuO}_{6+\delta}$.** **a, b** The refractivity **a** and absorption **b** as a function of laser wavelength. The red and purple arrows indicate 800 nm and 400 nm laser, respectively.



Supplementary Figure 6. **Photoinduced dynamics at different momenta with excitation of 800 nm and 400 nm.** **a**, **b** Time evolution of scattering intensity at Q_{CO} and away from Q_{CO} , with excitation of 800 nm (3 mJ/cm^2) in **a** and 400 nm (5 mJ/cm^2) in **b**. Intensities are normalized by the equilibrium scattering intensity.



Supplementary Figure 7. **CO dynamics in a long-time scan.** Time evolution of CO peak intensity over a delay time of 500 ps on a logarithmic scale, after the 400 nm pump with fluence of 5 mJ/cm^2 . Intensities are normalized by the equilibrium peak intensity.